

Optical Switch Based on $\text{Ge}_2\text{Sb}_2\text{Se}_4\text{Te}_1$ -Assisted Racetrack Microring

Yan Xu, Songyue Liu, Tingyu Liu, Yang Gao, Yuexin Yin , Xiaoqiang Sun *  and Daming Zhang 

State Key Laboratory of Integrated Optoelectronics, College of Electronic Science & Engineering, Jilin University, Changchun 130012, China; yanxu20@mails.jlu.edu.cn (Y.X.); sylu20@mails.jlu.edu.cn (S.L.); liuty20@mails.jlu.edu.cn (T.L.); ygao17@mails.jlu.edu.cn (Y.G.); yxyin20@mails.jlu.edu.cn (Y.Y.); zhangdm@jlu.edu.cn (D.Z.)

* Correspondence: sunxq@jlu.edu.cn; Tel.: +86-136-0430-4384

Abstract: In this work, we have proposed and designed a 1×1 optical switch based on the optical phase-change material, $\text{Ge}_2\text{Sb}_2\text{Se}_4\text{Te}_1$ (GSST), for GSST-assisted silicon racetrack microring. Its optical power can periodically be exchanged between the straight silicon waveguide and the GSST/Si hybrid racetrack waveguide due to the formed directional coupling structure. By changing GSST from the crystalline state to the amorphous state, the switch shifts from the ON state to the OFF state, and vice versa. With finite-difference time-domain method optimization, the proposed switch shows an extinction ratio of 18 dB at 1547.4 nm. The insert losses at the ON and OFF states are both less than 1 dB. The proposed switch unit has the potential to build an $N \times N$ switch matrix.

Keywords: optical switch; optical phase-change material; racetrack microring



Citation: Xu, Y.; Liu, S.; Liu, T.; Gao, Y.; Yin, Y.; Sun, X.; Zhang, D. Optical Switch Based on $\text{Ge}_2\text{Sb}_2\text{Se}_4\text{Te}_1$ -Assisted Racetrack Microring. *Photonics* **2022**, *9*, 117. <https://doi.org/10.3390/photonics9020117>

Received: 26 January 2022

Accepted: 17 February 2022

Published: 18 February 2022

Publisher's Note: MDPI stays neutral with regard to jurisdictional claims in published maps and institutional affiliations.



Copyright: © 2022 by the authors. Licensee MDPI, Basel, Switzerland. This article is an open access article distributed under the terms and conditions of the Creative Commons Attribution (CC BY) license (<https://creativecommons.org/licenses/by/4.0/>).

1. Introduction

Data traffic over the optical networks has been dramatically increasing at an exponential rate. The optical switch matrix is crucial for large-scale optical cross connect (OXC). Among different platforms, silicon photonics exhibit great promise in data centers, cloud computing and internet connections [1–3]. A silicon switch matrix can be constructed by the typically used microring (MR) and Mach–Zehnder interferometer (MZI) building block. However, for a switching unit based on the carrier dispersion effect or thermo-optic effect, the device length always reaches several hundreds of microns due to the limited refractive index (RI) change (<0.01). The enlarged chip size requires uniform and highly precise fabrication [4]. Moreover, a switch matrix unit based on the carrier dispersion effect can only provide moderate optical isolation, which implies that the crosstalk (CT) is improved, setting up a limitation on the scale of the switch matrix. Moreover, the total power consumption will increase exponentially in the large-scale switch matrix, accompanied with an unfavorable temperature increment. Therefore, the switch building block that could offer better fabrication uniformity, low static and dynamic power consumption is strongly needed in future OXC.

Low loss, low power consumption, compact size, and large extinction ratio are desired features of an integrated component when it is applied as a switching unit in the $N \times N$ switch array. There was a previous study of the broadband optical switching matrix with innovative technologies. The reported optical switch cell with a footprint $240 \mu\text{m} \times 9 \mu\text{m}$ shows an extinction ratio of ~ 13 dB, an insertion loss of less than 2 dB, a crosstalk of around 12 dB, and the bandwidth is over 150 nm [5]. In [4], the three-waveguide directional coupler with a size of $100 \mu\text{m} \times 180 \mu\text{m}$ constructs the 2×2 switch unit of a Benes network. The insert losses for the cross and bar states are 0.013 and 0.32 dB, respectively, while the CTs when at two states are -37 and -32 dB, respectively. In [6], the proposed switch matrix shows a low loss of 0.9 dB per off state ring and 2.0 dB per on state ring. Its bandwidth is no larger than 0.8 nm. In addition, MRR has been used in wavelength-selective optical

switching. In [3], the designed photonic switch shows an ER of ~ 20 dB at the resonance wavelength. Meanwhile, the excess losses at the through port and drop port are 0.9 dB and 2 dB, respectively.

Optical phase-change materials (O-PCMs), including two-dimensional O-PCMs of graphene [7,8], transition metal carbide/nitride [9], transition metal dichalcogenide [10], three-dimensional O-PCMs of VO_2 [11,12], $\text{Ge}_2\text{Sb}_2\text{Te}_5$ (GST) [3,13], and $\text{Ge}_2\text{Sb}_2\text{Se}_4\text{Te}_1$ (GSST), as well as indium tin oxide (ITO) [14,15], gradually play an important role in non-volatile integrated optical switches, modulators and computing. Different from devices built on classic electro-optic [16–18] or thermo-optic [19–21] effects, switches based on O-PCMs rely on the optical property change (e.g., refractive index change >1) caused by the transition between amorphous (a-) and crystalline (c-) states. Therefore, the incorporation O-PCM and silicon photonics could compensate for the disadvantages of chip size, power consumption and non-volatility in silicon switches.

As a novel phase change material, GSST has attracted remarkable attention owing to its considerable optical characteristic variations in the amorphous and crystalline states. Compared to GST, GSST has an excellent optical figure of merit (FOM) improvement over two orders of magnitude, unprecedented broadband optical transparency [22]. The material, therefore, represents a new class of O-PCMs where the phase transition only triggers refractive index modulation but without the loss penalty. The GSST-assisted switch is non-volatile and self-holding, which ensures its stable function in large-scale switching matrices. Since power consumption only happens during the phase change process, the elimination of static power consumption allows for the low-power operation of the GSST switch, compared to the case based on the TO effect or carrier dispersion effect. This advantage of power saving is more apparent when the switching status has no change for a long time. In order to improve switch performances, different switch structures have been extensively studied. Compact footprints and sharp spectral selectivity are the most significant advantages of the MRR switch [3,23–27]. For example, a 1×1 wavelength-selective optical switch based on GST-assisted all-pass MRR demonstrates an extinction ratio (ER) of 12.5 dB and an insert loss of 2.5 dB [25]. Comparatively, the wider bandwidth (BW) can be expected in the directional coupler (DC) [4] or Mach–Zehnder interferometer (MZI) structure [28]. Therefore, MRR and compact DC structures are supposed to be combined with each other for a better solution.

In this paper, a 1×1 optical switch constructed by a straight silicon waveguide and a GSST-loaded (GSST/Si) racetrack MRR is theoretically demonstrated. The phase-matching in the formed DC structure can be fulfilled when GSST is in the amorphous state. The resulting strong coupling causes the peak resonance to decrease at the output port of straight GSST-loaded waveguide. When the GSST transfers to the crystalline state, the phase mismatch weakens the coupling effect in the DC structure, which results in the power increasing at the output port of the straight GSST-loaded waveguide. The proposed switch can work within a broad bandwidth, which offers it good potential in on-chip switching matrix construction.

2. Principle and Design

The mature O-PCM of GSST has the advantages of fast crystallization, large resistance and favorable refractive index change between amorphous and crystallization states. The crystallization of GSST can be realized within several ns, which makes it ideal for an application in optical switching. A GSST film may transform from the amorphous state to the face-centered cubic crystallized state, accompanied by a reduction in square resistance. The full transformation to a hexagonal structure causes a further decrement in resistance. Then, the resistance is maintained when the temperature is over the threshold. Therefore, the optical characteristics of the GSST/Si hybrid waveguide, including the mode field distribution, propagation constant and optical absorption are different from those of the traditional Si waveguide. The mode coupling and transmission are supposed to be studied to determine the key parameters of the hybrid waveguide.

2.1. Switch Structure

The proposed optical switch is shown in Figure 1. The GSST thin film covers one race of the MRR that neighbors to another straight silicon waveguide. These two neighbored waveguides construct a DC coupler that could offer a relatively long coupling length. The phase-matching condition is satisfied between the racetrack and the straight waveguide when GSST is in the amorphous state. The optical input will couple to the ring, and the output power in the straight waveguide decreases dramatically at the resonance wavelength, which corresponds to the OFF state. When GSST is in the crystalline state, the resulting phase mismatching causes no power exchange between the two waveguides. The input power will directly output from the straight waveguide that corresponds to the ON state.

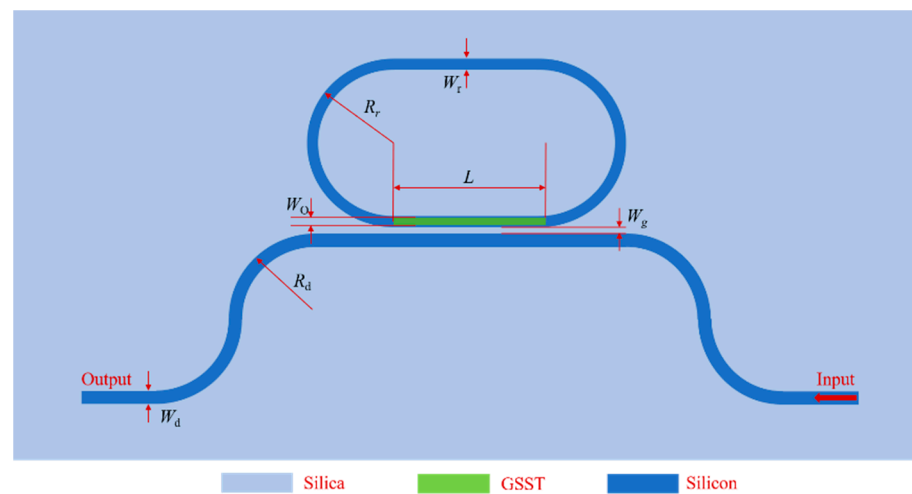


Figure 1. Schematic configuration of the proposed 1×1 optical switch based on a GSST-assisted racetrack MRR.

2.2. Switch Optimization

2.2.1. Single-Mode Waveguide

In this work, 220 nm thick top silicon and 2 μm thick silicon oxide are used as the waveguide core and lower cladding. The refractive indices of silicon and silica are 3.467 and 1.444 ($\lambda = 1550$ nm), respectively. The complex refractive indices of GSST are $3.375 + 0.00018i$ in the amorphous state and $5.0 + 0.42i$ in the crystalline state, respectively [4]. Compared with the traditional silicon waveguide, the propagation loss of an O-PCM-assisted silicon waveguide will show a higher loss, because the imaginary part (corresponding to the attenuation coefficient) of the complex refractive index of PCM will increase. Owing to this issue, it is desirable to enhance the coupling between the racetrack MRR and the bus waveguide, which will theoretically increase the ER. The notch depth is related to both to the racetrack MRR roundtrip loss and the power coupling coefficient between the ring and bus waveguide [29]. In this work, the radius R_d was set as 5 μm to increase ER. The bending radius we have chosen is much larger than the waveguide width ($R_d \geq 10 \times W_d$). Hence, the bending loss caused by the waveguide bending can be ignored. Additionally, the radius R_r in the racetrack MRR is set as 10 μm to reduce the bending loss as far as possible.

As mentioned above, the DC structure is designed to satisfy the phase-matching requirement, which means that the GSST covered-waveguide and straight silicon waveguide have similar effective refractive indexes (n_{eff}), when GSST is in the amorphous state. The three-dimensional finite-difference time-domain (3D-FDTD) method is used to simulate and optimize the switch design [3]. Firstly, the n_{eff} of the straight silicon waveguide as a function of its width W_d is calculated and shown Figure 2. For a low-loss single-mode prop-

agation, W_d is selected to be 500 nm. The inset shows the mode distribution at $n_{\text{eff}} = 2.445$.

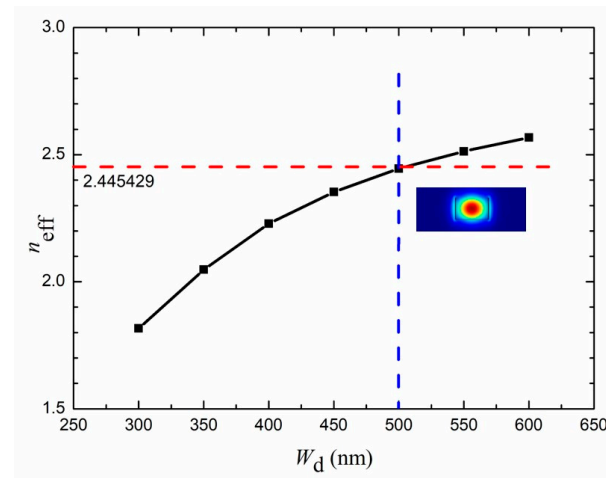


Figure 2. Effective refractive index n_{eff} as a function of silicon straight waveguide W_d .

Then, the geometric parameter of GSST-assisted racetrack MRR is investigated. Notably, the silicon ring has a consistent waveguide width W_r . The GSST film width W_O and thickness T_O are studied to satisfy the phase-matching condition. Here, W_r and T_O are chosen to be 450 nm and 45 nm, respectively, to improve the calculation efficiency. The result of n_{eff} as a function of W_O is shown in Figure 3. When W_O is 300 nm, the n_{eff} of the GSST covered silicon waveguide is 2.444, which is very close to that of the straight silicon waveguide. The insert picture shows that the single-mode intensity profile W_O is 300 nm.

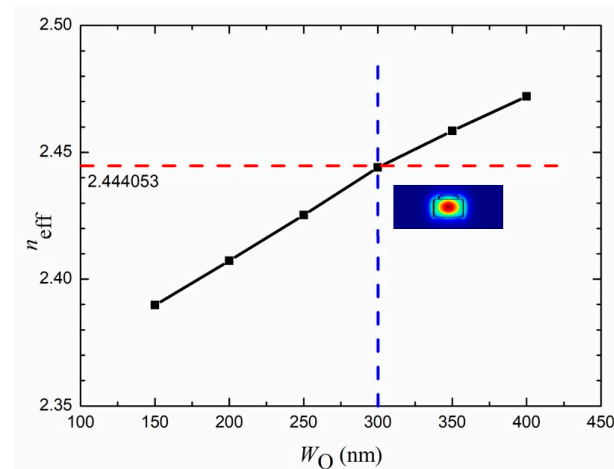


Figure 3. The relation of effective refractive index and the width of GSST W_O .

2.2.2. DC Structure

Following finite-difference eigenmode calculations, the modal intensity profiles of the GSST-loaded silicon waveguide in the amorphous state and in the crystalline state are shown in Figure 4a,b, respectively. In the crystalline state, GSST with a sufficiently high index leads to more mode power distribution in the GSST layer, as shown in Figure 4b. In contrast, the mode field mainly distributes in the silicon waveguide when GSST is in the amorphous state.

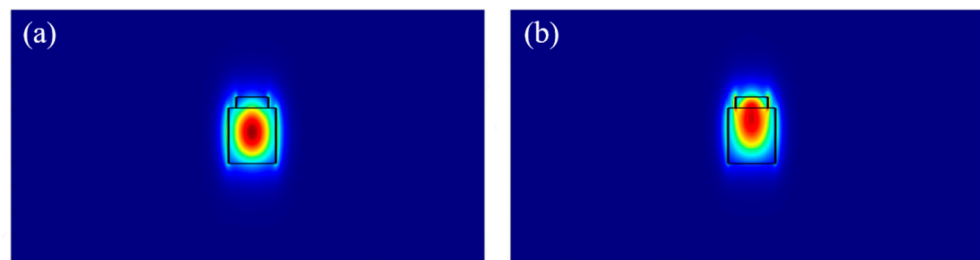


Figure 4. The modal intensity profiles of a silicon waveguide loaded with a GSST strip in the (a) amorphous and (b) crystalline states.

The TE-polarized supermodes profiles in two DC waveguides, the GSST-loaded silicon waveguide and the silicon waveguide without GSST, are shown in Figure 5. When the GSST is in the amorphous state, the phase matching leads to a strong coupling between the two waveguides with well-defined even (symmetric) and odd (antisymmetric) supermodes, as shown in Figure 5a,b. In contrast, the large effective index disparity between the two waveguides when GSST is in the crystalline state results in two isolated modes, as shown in Figure 5c,d. Therefore, by tuning GSST states, the supermodes can be separated into two independently propagating modes in the GSST-loaded silicon waveguide and the silicon waveguide without GSST, which implements the optical switching.

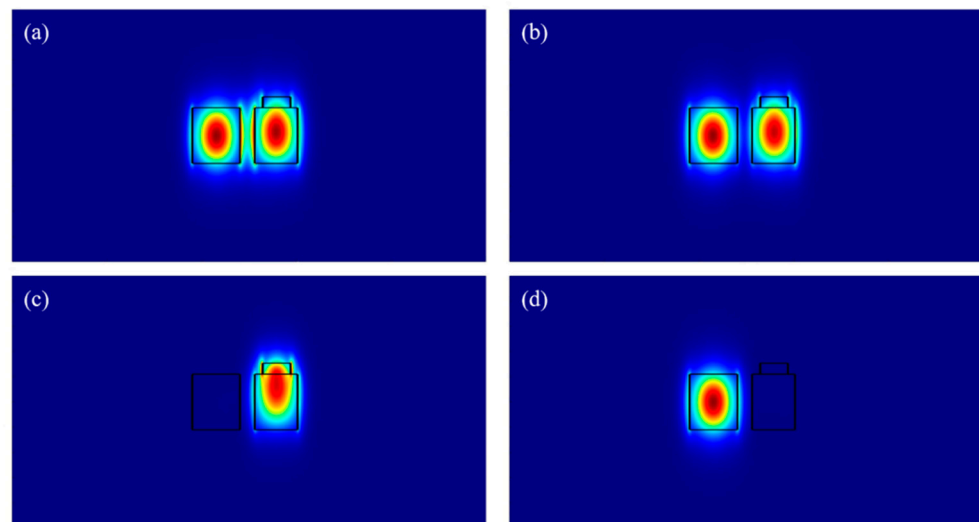


Figure 5. Intensity profiles of (a) even and (b) odd supermodes in the DC coupler waveguides when GSST is in the amorphous state; (c,d) show the mode distribution in DC coupler waveguides when GSST is in the crystalline state.

For better switching performance, the major parameters, including the coupling length L and the gap width W_g are supposed to be optimized. For simulation efficiency, the finite difference eigenmode is first adopted for a coarse search. Then, 3D-FDTD calculations are used to further refine the results to determine the best parameters. Figure 6 shows the normalized transmission in the racetrack MRR as a function of the coupling length L , when the launched TE mode propagates through the DC coupler. The gap width W_g is first chosen as 175 nm, which is sufficiently close for coupling. Here, the amorphous and crystalline states are considered, respectively. It can be seen that the power in the racetrack MRR increases firstly when GSST is at the amorphous state. Then, it decreases with the increment of L , which can be expected in a coupling system with two phase-matched optical waveguides. In contrast, when GSST is in the crystalline state, weak cross-coupling happens. Most power stays in the straight silicon waveguide, which is due to the phase

mismatching between the two optical waveguides. Hence, L is compromisingly selected to be 15 μm .

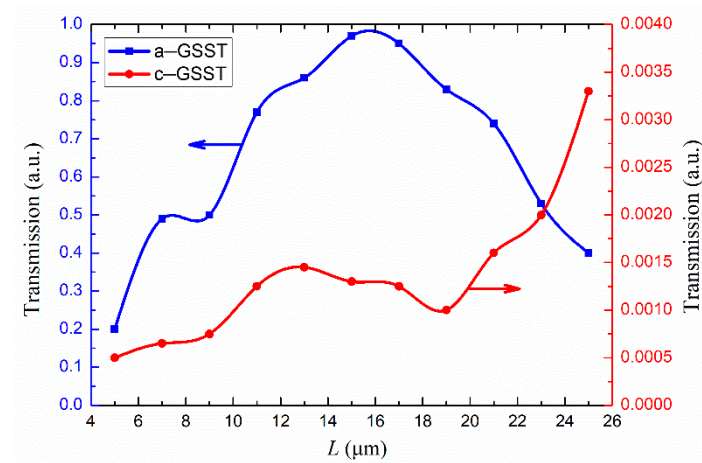


Figure 6. Normalized transmission of TE mode in racetrack MMR as a function of the coupling length L , when GSST is in amorphous and crystalline states, respectively.

With the same method, the remaining power in the racetrack MRR are investigated as a function of the DC coupler gap W_g , when GSST is in the amorphous and crystalline state, respectively. As shown in Figure 7, when GSST is in the amorphous state, the transmission in racetrack MRR increases to the highest value of 0.95 at $W_g = 125$ nm, which corresponds to strong coupling, and the least power remains in the straight silicon waveguide. When W_g is larger than 125 nm, the transmission reduces with the increment of W_g , which implies that the coupling weakens, and most power remains in the straight silicon waveguide. When GSST is in the crystalline state, the failed phase matching leads to a few power exchanges in the DC structure. Most input optical power remains in the straight silicon waveguide. Considering the fabrication feasibility and the strongest coupling, W_g is selected as 125 nm.

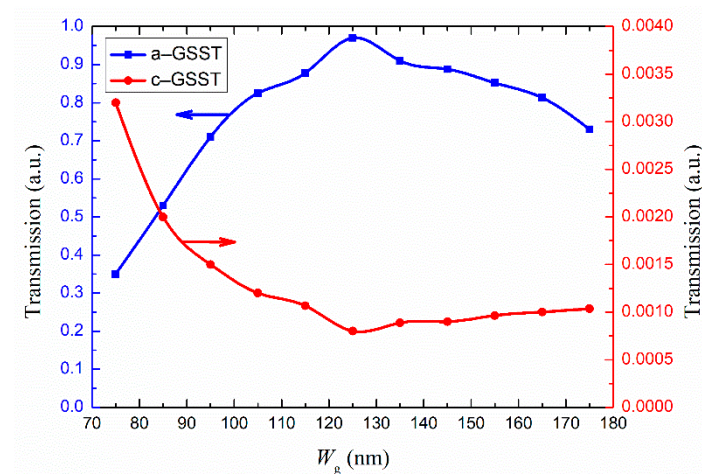


Figure 7. Normalized transmission in the racetrack MMR as a function of DC coupler gap W_g , when GSST is in amorphous and crystalline states, respectively.

To be noted, according to the relationship between Q factor and W_g , when strong resonances happen at certain wavelengths, there is no direct connection between Q factor and W_g , unless the resonance between the microring and the bus waveguide is very weak. In that case, W_g that can be represented by the coupling coefficient will become the key factor to determine the coupling. In fact, Q may change with W_g , which is attributed to the variation in the coupling coefficient between the ring and bus waveguide [30].

3. Results and Discussion

With the above optimized dimensional parameters, the switching performance was theoretically investigated by the 3D-FDTD method. The simulated optical power distributions in the OFF (a-GSST) and ON (c-GSST) states are shown in Figure 8a,b, respectively. As shown in Figure 8a, when GSST is in the amorphous state, most input light power couples to the racetrack MRR at the resonance wavelength 1547.4 nm. As shown in Figure 9, for the case of 150 μm long switch, the resonance depth and insertion loss (IL) are -18.861 dB and -0.187 dB, respectively. The loss mainly originates from the absorption of amorphous-state GSST. When GSST is in the crystalline state, almost no resonance oscillation can be observed in the MMR, which originates from the phase mismatching induced by the refractive index change in GSST, as shown in Figure 8b. The extinction ratio based on the resonance depths difference between two states is about -18 dB.

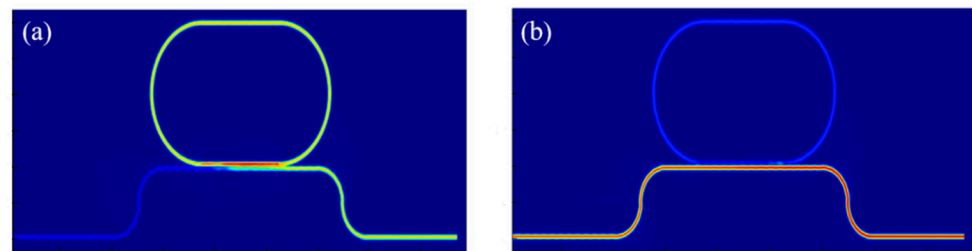


Figure 8. Optical power distribution of the designed switch simulated by the 3D-FDTD method at resonance wavelength near 1547.4 nm in (a) a-GSST (OFF) and (b) c-GSST (ON) states.

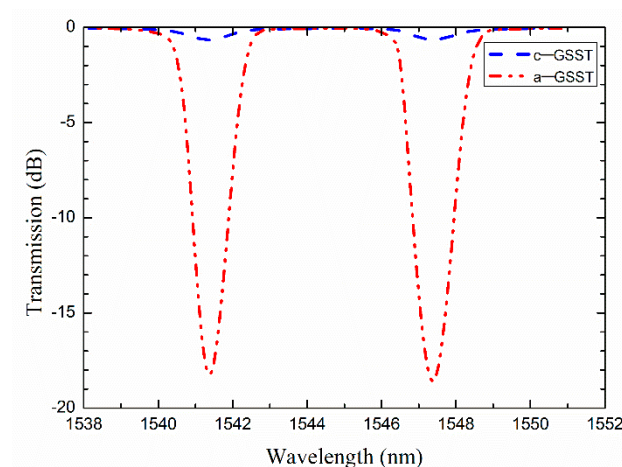


Figure 9. Spectral response of proposed MRR switch when GSST is in amorphous and crystalline states.

As shown in Figure 9, the 3 dB bandwidth of the proposed switch is ~ 1 nm. No obvious resonance wavelength shift occurs in different GSST states. Notably, dual resonance peaks with a distance ~ 6.04 nm can be observed here. This phenomenon is different from the reported single-waveguide GST-based MRR switches, in which GST is embedded in the cavity and a remarkable wavelength shift is unavoidable [3]. Compared to the present optical switches that adjust the operation wavelength by laser trimming or thermal tuning [3], the dual resonance wavelengths make it possible to be extended for low-loss higher-port $N \times N$ arrays. Importantly, according to the features of the different network architectures of S&S, PILOSS, Crossbar and Benes, the specific switch metrics are supposed to be built on practical demands. However, the size of traditional switching metrics construction will increase remarkably with the enlargement in array scale. One possible solution is to avoid using large-size switching blocks. Directly introducing PCM to the active arm of the silicon waveguide to implement the ON/OFF of the optical path can effectively reduce the unit size. Another solution is to introduce the inter-layer coupling, which changes the signal routing from one-dimension to two- or three-dimension [31,32].

To better evaluate the proposed switch, its theoretical performance was compared to that of other O-PCM switches. Since these designs are built on different material platforms and principles, it is hard to conduct an evaluation with unified standards. Nevertheless, the comparison is implemented in terms of insertion loss, operation wavelength, bandwidth, and extinction ratio. As shown in Table 1 below, GST and MRR are adopted in [3,25]. Compared with these two designs, a wider bandwidth and lower insertion loss can be realized by our proposed switch; meanwhile, a close extinction ratio can also be obtained. Compared to [4], which adopts a DC structure through a higher insertion loss is with this work, better bandwidth and extinction ratio performances are fulfilled. Though a far larger bandwidth can be realized with the plasmonic waveguide structure in [11], it has a much lower insertion loss than that in this work.

Table 1. Switching performance comparison with reported works.

O-PCM	Structure/Effect	IL	BW (nm)	λ (nm)	ER (dB)	Ref
GSST	DC	0.4 dB/40 μm 0.06 dB/40 μm	NA	1550	NA	4
GST	MRR	0.9 dB/2 dB	NA	1563	~20	3
GST	MRR	2.5 dB	~0.1	1550	12.5	25
VO ₂	Plasmonic	4.15 dB	76	1550	18	11
This work (GSST)	MRR	0.862 dB/100 μm 0.187 dB/150 μm	~1	1547.4	~18	

Limited by lab facilities, we simply propose a possible switch fabrication process in this study. Firstly, the silicon waveguide ring could be formed by e-beam lithography and sequential inductively coupled plasma etching. Next, polymethylmethacrylate resist (PMMA) is spin-coated on the wafer, and the area where GSST is supposed to be deposited is opened by another e-beam lithography and development. Since GSST film is on the MRR side, its size can be reasonably enlarged for the convenience of laser spot heating. As has been reported, GSST can be formed by radio frequency (RF) sputtering a stoichiometric Ge₂Sb₂Se₄Te₁ target. After the PMMA layer is removed, the silica upper cladding can be deposited on top of silicon waveguide by plasma-enhanced chemical vapor deposition.

Optical irradiation [33–35] and electrical heating [36–38] have been adopted to realize the transition between amorphous and crystalline states. The optical irradiation heating works via a free-space laser, which is driven by electrical current. The electrical pulses with a tunable length and amplitude can be generated with a function generator and amplified by a high-gain amplifier, before implanted to the laser. The output optical pulses may be coupled into an SME, collimated, and focused down to the sample using an objective. In contrast, electrical heating via low-loss ITO electrodes, which can be directly placed on the top of GSST film, is driven by applying voltage. If without the upper-cladding, the electrode size can be greatly enlarged, which is much more convenient for operation. If the upper-cladding is over the silicon core, part of upper-cladding is supposed to be removed for the convenience of the metal electrodes and probes [25]. Therefore, the high-speed phase transformation between the amorphous and crystalline state in this GSST-assisted MRR waveguide can be triggered by heating the μm -scale spot with focused laser radiation at a wavelength of 975 nm [25], resulting in an optical switching. The switching performance could then be optimized by iteratively increasing the laser pulse time and power.

4. Conclusions

A 1×1 optical switch based on GSST-assisted silicon racetrack MRR has been theoretically proposed. The racetrack MRR and DC structure are designed and optimized by the FDTD method to meet the phase-matching condition. By tuning GSST between the crystalline and amorphous states, the output power from the straight silicon waveguide can be changed from an ON to OFF status. The proposed switch of $30 \mu\text{m} \times 55 \mu\text{m}$ shows

an extinction ratio of ~ 18 dB at the resonance wavelength. The insert losses at the ON state and OFF state are both less than 1 dB within the 3 dB bandwidth of 1 nm. No continuous power consumption is needed to maintain the switching state due to the nonvolatility of GSST. Therefore, the proposed switch can work within a broad bandwidth at a low power cost, giving it good potential in on-chip switching matrix construction.

Author Contributions: This work described in this manuscript is the collaborative development of all authors. Conceptualization and resources: D.Z.; formal analysis and investigation: Y.X.; validation: S.L.; data curation: T.L., Y.G. and Y.Y.; funding acquisition and writing—review and editing: X.S. All authors have read and agreed to the published version of the manuscript.

Funding: This study was supported by the National Key Research and Development Program of China (2019YFB2203001), National Natural Science Foundation of China (61675087).

Data Availability Statement: No applicable.

Conflicts of Interest: The authors declare no conflict of interest.

References

1. Ali, N.; Kumar, R. Mid-infrared non-volatile silicon photonic switches using nanoscale $\text{Ge}_2\text{Sb}_2\text{Te}_5$ embedded in silicon-on-insulator waveguides. *Nanotechnology* **2020**, *31*, 115207. [[CrossRef](#)] [[PubMed](#)]
2. Qin, G.; Zhu, Q.; Su, Y. Fast wavelength seeking in a silicon dual-ring switch based on artificial neural networks. *J. Lightwave Technol.* **2020**, *38*, 5078–5085. [[CrossRef](#)]
3. Zhang, C.; Zhang, M.; Xie, Y.; Shi, Y.; Kumar, R.; Panepucci, R.R.; Dai, D. Wavelength-selective 2×2 optical switch based on a $\text{Ge}_2\text{Sb}_2\text{Te}_5$ -assisted microring. *Photonics Res.* **2020**, *8*, 1171–1176. [[CrossRef](#)]
4. Zhang, Q.; Zhang, Y.; Li, J.; Soref, R.; Gu, T.; Hu, J. Broadband nonvolatile photonic switching based on optical phase change materials: Beyond the classical figure-of-merit. *Opt. Lett.* **2018**, *43*, 94–97. [[CrossRef](#)]
5. Brunetti, G.; Marocco, G.; Benedetto, A.D. Design of a large bandwidth 2×2 interferometric switching cell based on a sub-wavelength grating. *J. Opt.* **2021**, *23*, 085801. [[CrossRef](#)]
6. Dasmahapatra, P.; Stabile, R.; Rohit, A. Optical Crosspoint Matrix Using Broadband Resonant Switches. *IEEE J. Sel. Top. Quantum Electron.* **2014**, *20*, 5900410. [[CrossRef](#)]
7. Sun, F.; Xia, L.; Nie, C.; Qiu, C.; Tang, L.; Shen, J.; Sun, T.; Yu, L.; Wu, P.; Yin, S. An all-optical modulator based on a graphene-plasmonic slot waveguide at 1550 nm. *Appl. Phys. Express* **2019**, *12*, 042009. [[CrossRef](#)]
8. Jafari, B.; Soofi, H.; Abbasian, K. Low voltage, high modulation depth graphene THz modulator employing Fabry-Perot resonance in a metal/dielectric/graphene sandwich structure. *Opt. Commun.* **2020**, *472*, 125911. [[CrossRef](#)]
9. Xiao, B.; Li, Y.; Yu, X.; Cheng, J. MXenes: Reusable materials for NH_3 sensor or capturer by controlling the charge injection. *Sens. Actuators B. Chem.* **2016**, *235*, 103–109. [[CrossRef](#)]
10. Wu, Q.; Chen, S.; Wang, Y.; Wu, L.; Jiang, X.; Zhang, F.; Jin, X. MZI-based all-optical modulator using MXene $\text{Ti}_3\text{C}_2\text{T}_x$ ($T = \text{F}, \text{O}, \text{or OH}$) deposited microfiber. *Adv. Mater. Technol.* **2019**, *4*, 1800532. [[CrossRef](#)]
11. Moradiani, F.; Seifouri, M.; Abedi, K.; Gharakhili, F. High Extinction Ratio All-Optical Modulator Using a Vanadium-Dioxide Integrated Hybrid Plasmonic Waveguide. *Plasmonics* **2021**, *16*, 189–198. [[CrossRef](#)]
12. Ooi, K.; Bai, P.; Chu, H.S.; Ang, L.K. Ultracompact Vanadium Dioxide Dual-Mode Plasmonic Waveguide Electroabsorption Modulator. *Nanophotonics* **2013**, *2*, 13–19. [[CrossRef](#)]
13. Liang, H.; Soref, R.; Mu, J.; Majumdar, A.; Li, X.; Huang, W.P. Simulations of Silicon-on-Insulator Channel-Waveguide Electro-optical 2×2 Switches and 1×1 Modulators Using a $\text{Ge}_2\text{Sb}_2\text{Te}_5$ Self-Holding Layer. *J. Lightwave Technol.* **2015**, *33*, 1805–1813. [[CrossRef](#)]
14. Babicheva, V.; Boltasseva, A.; Lavrinenko, A. Transparent conducting oxides for electro-optical plasmonic modulators. *Nanophotonics* **2015**, *4*, 165–185. [[CrossRef](#)]
15. Ma, Z.; Li, Z.; Liu, K.; Ye, C.; Sorger, V.J. Indium-Tin-Oxide for High-performance Electro-optic Modulation. *Nanophotonics* **2015**, *4*, 198–213. [[CrossRef](#)]
16. Lu, L.; Zhou, L.; Li, X. Low-power 2×2 silicon electro-optic switches based on double-ring assisted Mach-Zehnder interferometers. *Opt. Lett.* **2014**, *39*, 1633–1636. [[CrossRef](#)]
17. Koch, U.; Uhl, C.; Hettrich, H.; Fedoryshyn, Y.; Leuthold, J. A monolithic bipolar CMOS electronic-plasmonic high-speed transmitter. *Nat. Electron.* **2020**, *3*, 338–345. [[CrossRef](#)]
18. Heni, W.; Haffner, C.; Baeuerle, B.; Fedoryshyn, Y.; Josten, A.; Hillerkuss, D.; Niegemann, J.; Melikyan, A.; Kohl, M.; Elder, D.L.; et al. 108 Gbit/s Plasmonic Mach-Zehnder Modulator with > 70 -GHz Electrical Bandwidth. *J. Lightwave Technol.* **2016**, *34*, 393–400. [[CrossRef](#)]
19. Fang, Q.; Song, J.F.; Liow, T.Y.; Hong, C.; Kwong, D.L. Ultralow power silicon photonics thermo-optic switch with suspended phase arms. *IEEE Photonics Technol. Lett.* **2011**, *23*, 525–527. [[CrossRef](#)]

20. Lu, Z.; Murray, K.; Jayatilleka, H.; Chrostowski, L. Michelson Interferometer Thermo-optic Switch on SOI with a 50 Microwatt Power Consumption. *IEEE Photonics Technol. Lett.* **2015**, *27*, 2319–2322.
21. Chen, W.; Lu, H.; Li, S. Experimental demonstration of a flexible-grid 1×2 wavelength-selective switch based on silicon microring resonators. *Opt. Lett.* **2019**, *44*, 403–406. [\[CrossRef\]](#)
22. Zhang, Y.; Chou, J.B.; Li, J. Extreme Broadband Transparent Optical Phase Change Materials for High-Performance Nonvolatile Photonics. *Nat. Commun.* **2019**, *10*, 4279. [\[CrossRef\]](#)
23. Ophir, N.; Mineo, C.; Mountain, D.; Bergman, K. Silicon photonic microring links for high-bandwidth-density, low-power chip I/O. *IEEE Micro* **2013**, *33*, 54–67. [\[CrossRef\]](#)
24. Dong, P.; Qian, W.; Liang, H.; Shafiiha, R.; Feng, D.; Li, G.; Cunningham, J.; Krishnamoorthy, A.; Asghari, M. Thermally tunable silicon racetrack resonators with ultralow tuning power. *Opt. Express* **2010**, *18*, 20298–20304. [\[CrossRef\]](#)
25. Rudé, M.; Pello, J.; Simpson, R.E.; Osmond, J.; Roelkens, G.; Joe, J.G.M.; Tol, V.; Pruneri, V. Optical switching at 1.55 μm in silicon racetrack resonators using phase change materials. *Appl. Phys. Lett.* **2013**, *103*, 141119. [\[CrossRef\]](#)
26. Zheng, J.; Khanolkar, A.; Xu, P.; Colburn, S.; Deshmukh, S.; Myers, J.; Frantz, J.; Pop, E.; Hendrickson, J.; Doylend, J.; et al. GST-on-silicon hybrid nanophotonic integrated circuits: A non-volatile quasi-continuously reprogrammable platform. *Opt. Mater. Express* **2018**, *8*, 1551–1561. [\[CrossRef\]](#)
27. Stegmaier, M.; Ríos, C.; Bhaskaran, H.; Wright, C.D.; Pernice, W.H.P. Nonvolatile all-optical 1×2 switch for chip scale photonic networks. *Adv. Opt. Mater.* **2017**, *5*, 1600346. [\[CrossRef\]](#)
28. Zhang, H.; Zhou, L.; Xu, J.; Lu, L.; Chen, J.; Rahman, B. All-optical non-volatile tuning of an AMZI-coupled ring resonator with GST phase-change material. *Opt. Lett.* **2018**, *43*, 5539–5542. [\[CrossRef\]](#)
29. Porzi, C.; Falconi, F.; Parca, G. Fast-Reconfigurable Microwave Photonics Phase Shifter Using Silicon Microring Resonators. *IEEE J. Quantum Electron.* **2021**, *57*, 0600409. [\[CrossRef\]](#)
30. Taufiqurrahman, S.; Dicky, G.; Estu, T.T. Free Spectral Range and Quality Factor Enhancement of Multi-Path Optical Ring Resonator for Sensor Application. *ISFAP AIP Conf. Proc.* **2019**, *2256*, 020003.
31. Suzuki, K.; Konoike, R.; Yokoyama, N. Nonduplicate Polarization-Diversity 32×32 Silicon Photonics Switch Based on a SiN/Si Double-Layer Platform. *J. Lightwave Technol.* **2020**, *38*, 226–232. [\[CrossRef\]](#)
32. Konoike, R.; Suzuki, K.; Tanizawa, K. SiN/Si double-layer platform for ultralow-crosstalk multiport optical switches. *Opt. Express* **2019**, *27*, 21130–21141. [\[CrossRef\]](#)
33. Ríos, C.; Stegmaier, M.; Hosseini, P.; Wang, D.; Scherer, T.; Wright, C.D.; Bhaskaran, H.; Pernice, W.H. Integrated all-photonic non-volatile multi-level memory. *Nat. Photonics* **2015**, *9*, 725–732. [\[CrossRef\]](#)
34. Ríos, C.; Stegmaier, M.; Cheng, Z.; Youngblood, N.; Wright, C.D.; Pernice, W.H.; Bhaskaran, H. Controlled switching of phase-change materials by evanescent-field coupling in integrated photonics. *Opt. Mater. Express* **2018**, *8*, 2455–2470. [\[CrossRef\]](#)
35. Youngblood, N.; Ríos, C.; Gemo, E.; Feldmann, J.; Cheng, Z.; Baldycheva, A.; Pernice, W.H.; Wright, C.D.; Bhaskaran, H. Tunable volatility of $\text{Ge}_2\text{Sb}_2\text{Te}_5$ in integrated photonics. *Adv. Funct. Mater.* **2019**, *29*, 1807571. [\[CrossRef\]](#)
36. Kato, K.; Kuwahara, M.; Kawashima, H.; Tsuruoka, T.; Tsuda, H. Current-driven phase-change optical gate switch using indium–tin–oxide heater. *Appl. Phys. Express* **2017**, *10*, 072201. [\[CrossRef\]](#)
37. Farmakidis, N.; Youngblood, N.; Li, X.; Tan, J.; Swett, J.L.; Cheng, Z.; Wright, C.D.; Pernice, W.H.; Bhaskaran, H. Plasmonic nanogap enhanced phase-change devices with dual electrical-optical functionality. *Sci. Adv.* **2019**, *5*, 2687. [\[CrossRef\]](#)
38. Leonardis, F.D.; Soref, R.; Passaro, V.M.; Zhang, Y.; Hu, J. Broadband electro-optical crossbar switches using low-loss $\text{Ge}_2\text{Sb}_2\text{Te}_5$ phase change material. *J. Lightwave Technol.* **2019**, *37*, 3183–3191. [\[CrossRef\]](#)